



Influence of tunable pore size on photocatalytic and photoelectrochemical performances of hierarchical porous TiO₂/C nanocomposites synthesized via dual-Templating

He Wang^a, Huan Liu^a, Shulan Wang^{a,*}, Li Li^{a,*}, Xuan Liu^{b,*}

^a Department of Chemistry, School of Science, Northeastern University, Shenyang, 110819, China

^b Department of Materials Science and Engineering, Carnegie Mellon University, Pittsburgh, PA, 15213, USA



ARTICLE INFO

Keyword:

TiO₂/C
Pore size
Photocatalytic
Organic-inorganic
PEC

ABSTRACT

TiO₂/C nanocomposites with hierarchical porous framework were synthesized by the dual-template method with ice and silica as the hard template. Silica of different dimensions was used as the knob to modify the TiO₂/C pore structure and to control anatase-rutile transformation. The prepared TiO₂/C nanocomposites with pores at three different scales with micro-, meso- and macro-pores not only prohibited aggregation of nanoparticles but also shortened the transportation distance of charge carriers. TiO₂/C fabricated with 22 nm colloid silica as the template showed superior photocatalytic performances of 4.0 and 10.7 times of the commercial benchmark P25 under UV and visible light irradiation, respectively. The TiO₂/C composites also showed excellent photoelectrochemical (PEC) performances with the photocurrent density of 6.3 mA/cm² that is 11.2 times of the control sample. The results demonstrated that the silica dimension serves a significant role for optimization of the TiO₂/C microstructure including particle size, phase composition, surface area and thus improvement in photoelectrochemical and photocatalytic properties.

1. Introduction

TiO₂ has attracted considerable attentions for its applications in water cleaning, electronic device fabrication as well as energy conversion and storage due to its advantages such as low cost, high physicochemical stability and non-toxicity [1–4]. However, use of TiO₂ for solar energy conversion is still restricted by its wide band gap with poor visible light response, low quantum efficiency and limited mass diffusion [5–9]. To address these issues, many efforts have been devoted to tune the electrical/optical properties of TiO₂ and to reduce its photo-generated electron-hole recombination rate by metal or non-metal doping, surface modification and coupling of heterostructured semiconductors/conductors with a narrow band gap [1,10,11]. As an efficient electron acceptor, carbon conducts photo-generated electrons and depresses recombination of charge carriers. It is also lightweight, non-polar, non-reactive and nontoxic material with large-scale availability. Therefore, metal oxide/carbon composites are highly attractive as potential high performance photocatalysts [12]. Important requirements for high performance functional photocatalytic materials include a small particle size, a large surface area and robust chemical stability [13]. Particularly, porosity and the pore size distribution are crucial for

tuning their energy-related performances for charge carrier transport, ion diffusion, and structural buffering, etc [14]. In the current stage, efficient fabrication of hierarchical inter-connected pore structures at different length scales in metal oxide/carbon materials are still limited by techniques and methodology. Furthermore, effective control of the pore structure with high electrochemical properties is challenging. Metal oxo-clusters are commonly used for fabrication of materials with high functionality in fields of drug delivery, micro-optics, photovoltaic solar cell, lithium ion battery and supercapacitor, etc [15,16].

In the current work, we used metal oxo-clusters as precursors and fabricated TiO₂/carbon nanocomposites with inter-connected pore structures in three different scales by the dual templation method combining both ice and silica hard templates, and discussed corresponding influences on their photocatalytic and photoelectrochemical performances. Titanium oxo acetate clusters made via the sol-gel technique was used as the titanium source for size and stoichiometry control. Silica colloid with different SiO₂ particle sizes in this work was not only used for adjustment of the mesopore size of the interconnected hierarchical TiO₂/C nanocomposites, but also as a sacrificial template to form mesopores. NaOH etching is performed to remove the SiO₂ hard template and expand the mesopores [17–19]. The interconnected

* Corresponding authors.

E-mail addresses: s1wang@mail.neu.edu.cn (S. Wang), lilicmu@alumni.cmu.edu, lilicmu@gmail.com (L. Li), xuanliucmu@gmail.com (X. Liu).

hierarchical pores in the nanocomposite are of the long-range order while dimensions of silica significantly affect the pore structure of the TiO₂/C nanocomposites and also the anatase to rutile phase transformation of the TiO₂ component [20,21].

The TiO₂/C nanocomposites showed excellent photocatalytic reactivities for methylene blue (MB) degradation which are about 4.0 and 16.8 times of the benchmark photocatalyst P25 and anatase under UV light exposure. The TiO₂/C nanocomposites also showed excellent photoelectrochemical performances due to their appropriate pore structure for efficient transmission of photo-generated charge carriers as well as fast diffusion of adsorbents and electrolytes to the inner surface of the active materials. As far as we know, this is the first-reported work about the strategy in tuning the interconnected hierarchical pore structure of various scales in metal oxide/carbon nanocomposites for enhanced photocatalytic/photoelectrochemical performances. In addition to TiO₂, this method can also be applied in production of other materials with enhanced electrochemical performances for energy-related applications.

2. Experimental section

2.1. Photocatalyst preparation

Commercial tetraisopropyl titanate (99%, Aladdin Chemical Reagent Co., Ltd, China) was used as the Ti source for synthesis of titanium oxo clusters. Glacial acetic acid (AR, Yong Da Chemical, Tian Jin, China) and tetraisopropyl titanate was first mixed with a volume ratio of 10:1 and then room-temperature stirred. The solution transformed into milky suspension and the precipitate collected by centrifugation followed with vacuum drying at 65 °C to obtain the white powder (noted as TOA). 0.8 g TOA was mixed with 0.3 g sucrose (AR, Xin Hua Chemical, Shen Yang, China) and the corresponding amount of colloid silica solution with SiO₂ diameter of 22 nm, 12 nm and 7 nm (Lodox, Sigma Aldrich, 40 wt%, 30 wt% and 30 wt%) to guarantee that the mass ratio between sucrose and SiO₂ is 1:1, respectively. Subsequently, 3 mL deionized water was added to dissolve the mixture and formed a jelly-like transparent solution. The solution was fast frozen by using liquid nitrogen and then freeze-dried for 12 h. White powders were collected after freeze-drying and annealed at 900 °C for 5 h in Ar atmosphere for preparation of TiO₂/C nanocomposites. SiO₂ was removed by etching with 3 M NaOH solution at 80 °C for 24 h. The samples were then neutralized by deionized water for adjustment of the pH value. The samples were designated as TCS22, TCS12 and TCS7, respectively, which are used to represent TiO₂/C nanocomposites prepared from etching silica of different sizes. The samples without SiO₂ addition, noted as TCS0, were used as the control sample. In addition, commercial P25 (Degussa) and anatase were added into the control group. Influence of the annealing time and temperature on the photocatalytic activity was also conducted.

2.2. Photocatalytic and photoelectrochemical characterization

The photocatalytic activity of prepared nanocomposites was investigated via measurement of the degradation curve in the MB solution (Shenyang Chemical Reagent Co. Ltd., P.R. China.) under UV/visible light exposure. A 125 W high-pressure mercury lamp and a 300W Xe lamp (PLS-SXE 300) with an UV filter were used as light sources. 25 mg of TiO₂/C composite was added into 80 mL 10⁻⁴ mol/L MB solution in a stirred quartz reactor. The photocatalytic experiments were conducted after a 30-min magnetic stirring session free of light exposure for a complete adsorption/desorption equilibrium state between catalyst and the solution. Under continuous stirring, 6 mL sample solutions were taken intermittently followed by centrifugation for complete removal of powders. Degradation of MB was evaluated by a UV-vis spectrophotometer at the maximum absorbance peak ($\lambda = 664$ nm) (Scheme 1).

For setup of photoelectrochemical measurement, 2 × 1 cm FTO

glass was cleaned by acetone, ethyl alcohol and water successively before analysis. A few drops of N-methyl pyrrolidone (NMP) solution were then added into TiO₂/C powders, followed by continuous stirring to form a uniform paste that is then spin-coated on the surface of FTO with the subsequent drying at 80 °C. The thickness is about 100 μm.

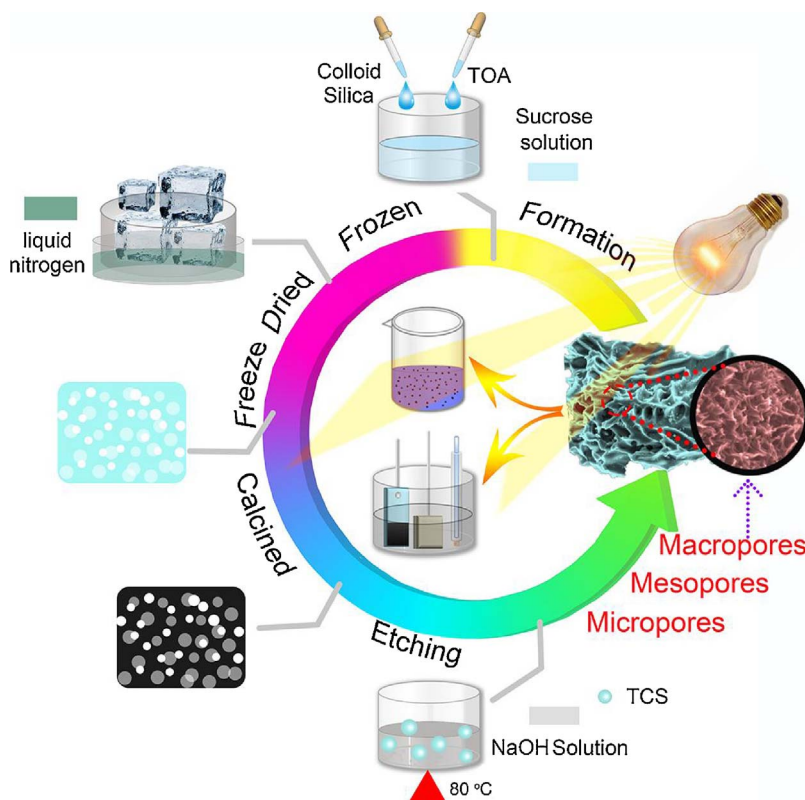
The TiO₂/C served as the working electrode while Pt as the counter electrode. A saturated calomel electrode (SCE) worked as the reference electrode. Photocurrent measurement was carried out under visible light irradiation using a high-pressure xenon lamp. Electrochemical measurements were performed in 1 M Na₂SO₄ solution with linear sweep voltammetry swept linearly the voltage range between 0 and 1.0 V vs the reference electrode with a scan rate of 50 mV·s⁻¹. Photocurrent is affected by many factors such as light intensity and amount of catalysts, et al. The visible light intensity in all our experiments is 250 mW/cm² with an AM 1.5G filter. Detailed experimental setup for material synthesis and evaluation of photocatalytic/photoelectrochemical performances is shown in Schematic 1.

2.3. Materials characterization

X-ray diffraction (XRD) patterns were collected from X' Pert Pro diffractometer (PANalytical B.V., Netherlands) and were used to analyze the phase composition of samples. Raman spectra were recorded using (I Horiba Jobin Yvon LabRAM HR 800, French) with a laser excitation wavelength of 532 nm from 800 to 3500 cm⁻¹. Thermogravimetric and differential thermal analysis (TG/DTA, METTLER TOLEDO-3) of the TiO₂/C precursor was carried out in N₂ with a heating rate of 10 °C/min between 25 and 1100 °C. UV-vis diffuse reflectance spectroscopy (DRS) was used with a Lambda 35 UV/VIS spectrometer equipped with an integrating sphere attachment from 200 to 800 nm for evaluation of light absorption. Surface groups in the samples were investigated using a Fourier transform infrared spectroscopy (FT-IR) spectrometer (Perkin-Elmer 843). Surface morphology and elemental distribution were studied using the scanning electron microscope (SEM) and energy-dispersive spectroscopy (Ultra Plus, Carl Zeiss, Germany). Transmission electron microscopy (TEM, JEM-2100) was conducted at an accelerating voltage of 200 kV to study the microstructure under high resolution. Porosity of the samples was evaluated through Brunauer-Emmett-Teller (BET) analysis from desorption data with the pore volume measured at P/P₀ = 0.99 point, as well as the nonlocal density functional theory (NLDFT) method with N₂ as adsorptive (77 K).

3. Results and discussion

The XRD patterns of TiO₂/C with SiO₂ of different sizes were shown in Fig. 1a. All the sharp and narrow diffraction peaks in the XRD patterns can be exclusively ascribed to TiO₂/C crystals of anatase (01-073-1764) and rutile (01-078-1510) of different ratios. No impurity peaks detected from Fig. 1a. Dimension of SiO₂ influenced the percentage of anatase in the samples and played a contradictory role in transformation of anatase into rutile. Percentage of rutile decreased from 65% in TCS0 to 62.6%, 33.9% and 24.3% in TCS7, TCS12 and TCS22, respectively. In other words, the anatase content increased with increase in the SiO₂ dimension. The crystallite size of anatase and rutile was calculated based on Scherrer's equation with results displayed in Table 1. Carbon doping can lead to the lattice cell expansion because of the large atom radius of C [22]. Meanwhile, the silica addition can influence the phase transformation between anatase and rutile. After addition of colloid silica the crystalline size decreased in rutile but increased in anatase. The lattice parameters and cell volume of TiO₂/C nanocomposites with colloid silica of different sizes as the hard template annealed at 900 °C are shown in Table S1. A slight increase in lattice parameters and volume of both anatase and rutile compared with standard samples can be observed, confirming doping of C into the TiO₂ matrix.



Raman spectra of the samples were collected to investigate the carbon status of the nanocomposites (Fig. 1b). Two characteristic peaks, D and G bands at 1346 and 1580 cm^{-1} , are ascribed to the disorder carbon and graphite carbon, respectively [23]. The value of I_D/I_G , which was 1.096, 1.064, 1.043, 0.992 for TCS22, TCS12, TCS7 and T-CS0, slightly increased with increase in the silica size. This result indicates slight increase in the graphitization degree with decrease in silica size added into the nanocomposites [24]. The presence of graphite with high conductivity can retard the recombination of photo-generated charge carriers in the photoactive component (TiO_2) and thus can enhance the photochemical reactivity of the nanocomposites.

To further evaluate the interaction between carbon and TiO_2 as well as their thermal properties, TG-DTA of the TiO_2/C precursor after freeze drying were conducted under N_2 flow with results shown in Fig. 2a. The weight loss curve can be divided by different physicochemical changes in the TiO_2/C samples into two stages. In the first stage with temperatures lower than 125 °C, the samples lost adsorbed water molecules accompanied by degradation of redundant acetate, resulting in the endothermic peak at 125 °C. In the second stage at temperatures between 125 and 500 °C, organic ligands decomposed and TiO_2 was

Scheme 1. The synthetic flow of hierarchical porous TiO_2/C nanocomposites with dual templation method and the corresponding photochemical characterization.

Table 1

Crystallite size and phase composition of TiO_2/C nanocomposites with colloid silica in different sizes as hard template annealed at 900 °C.

Samples	Phase Composition (%)		Crystallite Size (nm)
	Rutile	Anatase (101)	
TCS0	65	10.5	20.3
TCS7	62.6	14.2	18.4
TCS12	33.9	12.5	13.1
TCS22	24.3	12.0	11.9

formed, accompanied by weight loss of 40%. The primary exothermic peak in Fig. 2a at 370 °C represents decomposition and carbonization of organic ligands. The exothermic peak at 750 °C corresponds to TiO_2 phase transformation [25,26].

Surface organic groups of the TiO_2/C precursor before annealing and after etching were analyzed by FT-IR with results in Fig. 2b. The broad peak at 3320 cm^{-1} and the sharp peak at 924 cm^{-1} in the FT-IR spectra of the TiO_2/C precursor before annealing are related to the

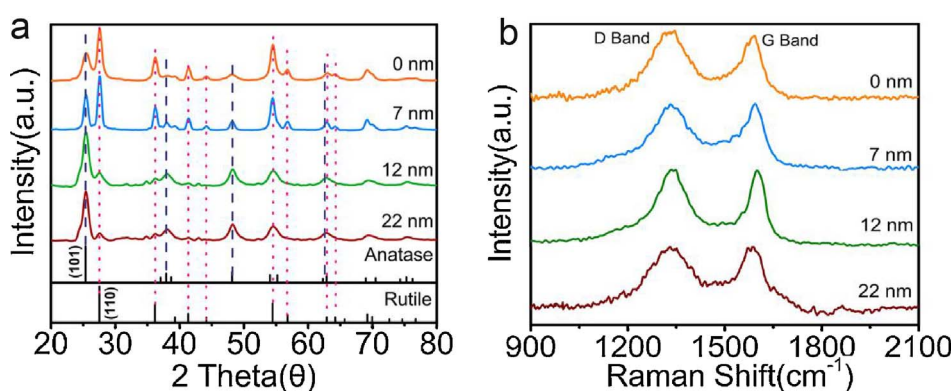
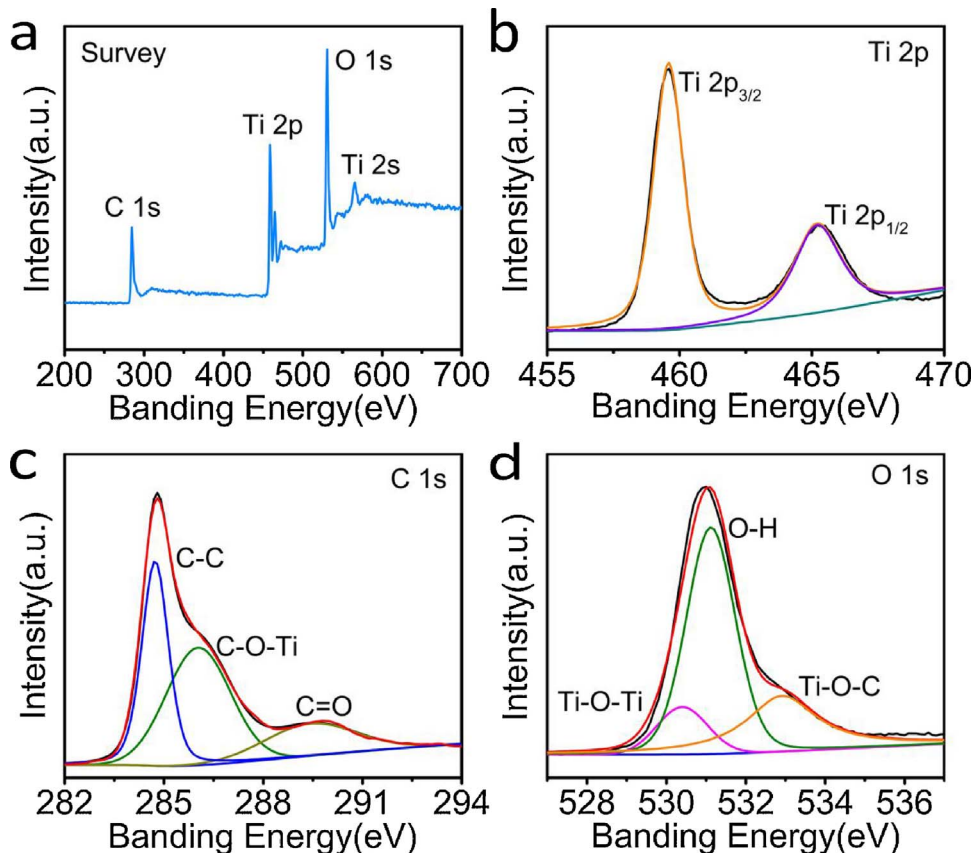
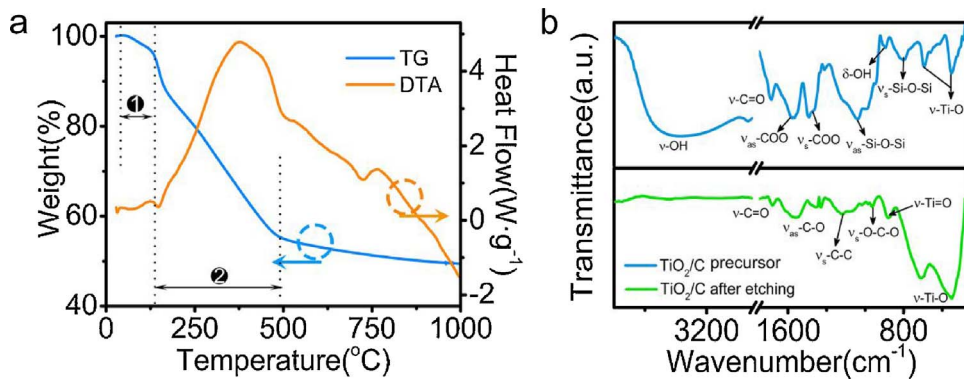


Fig. 1. (a) XRD pattern and (b) Raman spectrum of TiO_2/C nanocomposites with colloid silica in different sizes as the hard template annealed at 900 °C.



stretching vibration and deformation vibration of O—H (intermolecular H-bonds, polymeric), respectively. Furthermore, the peak at 1733 cm^{−1} is related to the carbonyl and carboxylic groups (ν —C=O) [27]. The peaks at 1557 and 1426 cm^{−1} in the spectrum are attributed to the asymmetric (as) and symmetric (s) stretching bands of —COO. This peak serves as a good indicator of chemical bonding between the TiO₂ core and the ligands. Existence of the Si—O bond is confirmed by peaks at 1116 and 797 cm^{−1}, indicating formation of the Si—O—Si stretching vibration bands [28,29]. The other two noticeable peaks at 661 and 464 cm^{−1} are the characteristic peaks of isopropyl titanate. In contrast, all peaks related to organic ligands observed previously in the TiO₂/C precursor disappeared in the FT-IR spectrum after annealing and etching. The prominent peaks observed at 1539, 1219, 1022 cm^{−1} come from C—C and C—O, the strong chemical bonds between carbon and TiO₂. The characteristic peaks at 400–700 cm^{−1} are accredited to stretching of Ti—O and Ti—O—Ti [30,31]. No Si—O peaks are observed, meaning complete removal of silica in the nanocomposites. As shown in Fig. S1, light absorption was investigated by UV-vis diffuse reflection

spectra. Compared with the control sample P25, all TiO₂/C samples showed visible light response because the successful carbon doping narrowed the band gap of TiO₂, while the band gap change due to the different percentage of anatase and rutile are negligible.

In Fig. 3a, the specific chemical state of TiO₂/C nanocomposites with 22 nm colloid silica as the template was characterized by X-ray photoelectron spectroscopy (XPS). As shown in Table S2, the elemental composition of TCS22 is 27.2% C, 48.6% O, 11.1% Si and 13.1% Ti before etching while no Si is observed after NaOH etching. As presented in Fig. 3a, the full XPS survey, no elements are detected other than Ti, O and C. The Ti 2p spectrum in Fig. 3b can be divided into two primarily peaks at 459.6 and 465.3 eV, respectively, that are related to Ti 2p_{3/2} and Ti 2p_{1/2} [32,33]. In Fig. 3c, the C 1s spectrum, the main peak located at 284.7 eV corresponds to the C—C bond, while the peak at 285.9 eV is related to Ti—O—C, which suggests establishment of the chemical bonding interaction between TiO₂ and carbon in the nanocomposites [34,35]. Another broad peak at 289.2 eV is attributed to the carboxyl COOH bonds on the surface. In Fig. 3d, the O 1s peak can be

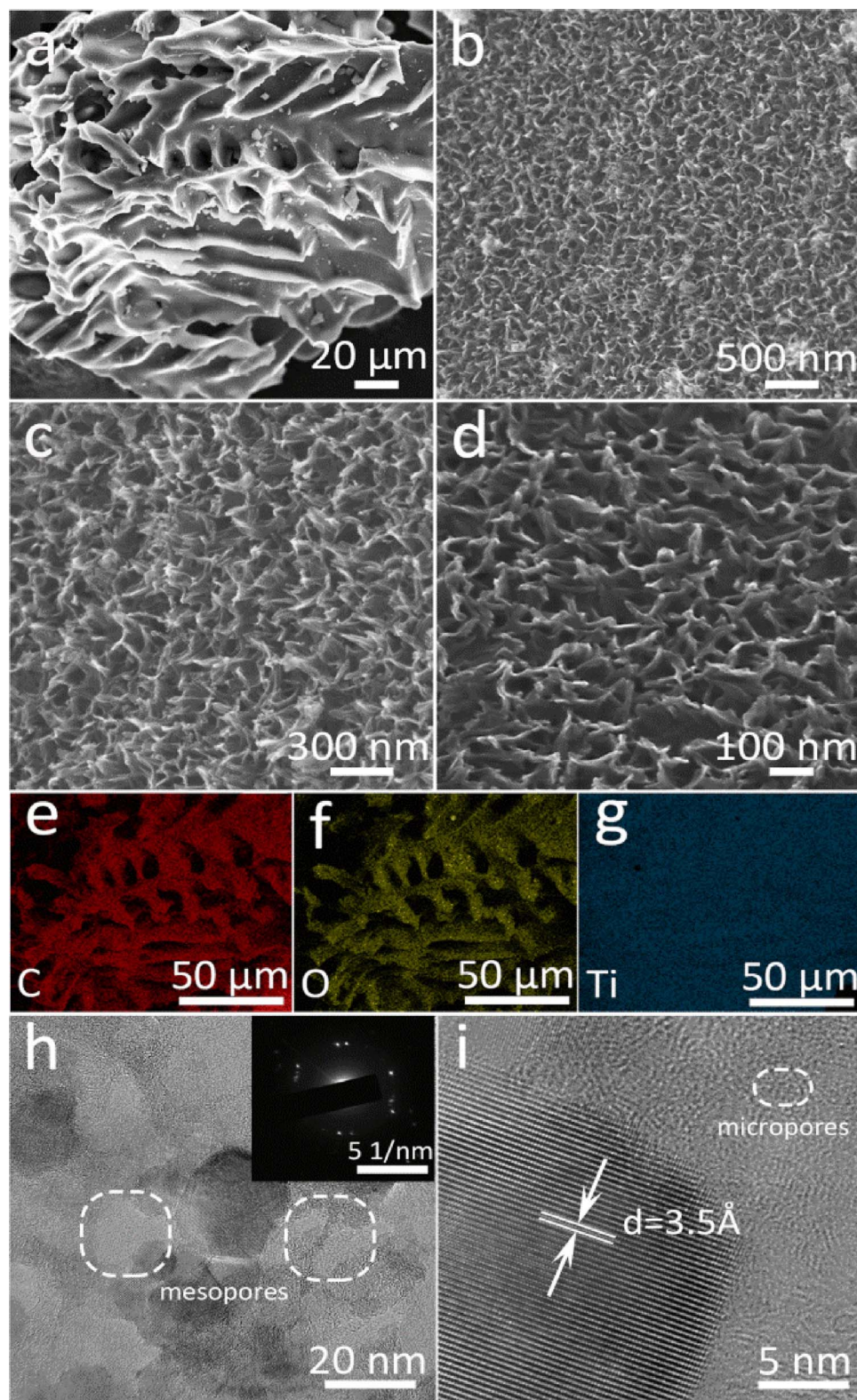


Fig. 4. TiO_2/C annealed at $900\text{ }^\circ\text{C}$ with the 22 nm silica template: (a, b, c, d) SEM images with different magnifications; (e-g) EDX mapping; (h) TEM bright field image with the selected area electron diffraction (SAED) pattern as the inset; and (i) high resolution TEM image with the lattice fringe of TiO_2 .

divided into three peaks, the Ti-O peak in the structure of TiO_2 at 529.9 eV, the O-H peak at 531.7 eV with the highest intensity, and the Ti-O-C peak at the binding energy of 532.8 eV [36–38]. Overall, these XPS readout strongly supports the conclusion that robust chemical interaction between TiO_2 and carbon has been formed. Meanwhile, Ti-O-C band in Fig. 3c and Ti-O/Ti-O-C peaks in Fig. 3d confirm that the substitutional carbon doping also exists, which is consistent with the

XRD and UV-vis result. The strong interaction enhances the charge transfer capability between the components and thus promote the photocatalytic activity by separation of photo-generated charge carriers [36].

As shown in Fig. 4a–d, surface morphology and microstructure of TiO_2/C annealed at $900\text{ }^\circ\text{C}$ with 22 nm colloid silica as the template (TCS22) were investigated by scanning electron microscopy (SEM) at

Table 2

Surface area and pore structure of the TiO₂/C nanocomposites with the silica template in different sizes.

Samples	S _{BET} (m ² g ⁻¹)	S _{micro} (m ² g ⁻¹)	S _{meso} (m ² g ⁻¹)	V _{pore} (cm ³ g ⁻¹)	V _{micro} (cm ³ g ⁻¹)	V _{meso} (cm ³ g ⁻¹)
TCS0	263	55	150	0.155	0.0193	0.113
TCS7	279	50	174	0.317	0.0183	0.291
TCS12	287	49	187	0.378	0.0126	0.353
TCS22	330	47	227	0.396	0.0115	0.379
Anatase	14	0	13	0.177	0	0.177
P25	54	0	51	1.088	0	1.088
P25/C	88	40	48	0.208	0.022	0.186

S_{micro} and S_{meso} correspond to surface areas of micropores and mesopores, respectively; V_{pore} is the total pore volume; V_{micro} and V_{meso} are volumes of micropores and mesopores.

different magnifications. The “fish-bone” structure with 20 μm interconnected macropores was formed while the wall of homogeneous TiO₂/C nanocomposites is composed of the mesopores, providing high surface area and sufficient reaction sites for pollutant decomposition. The SEM images of TCS0, TCS7 and TCS12 were also shown in Fig. S2. All samples with ice templation showed the similar “fish-bone” structure while different silica size led to the formation of different pore structures. Distribution of Ti, C and O in the TiO₂/C nanocomposite was analyzed by the energy dispersive X-ray (EDX) with results in Fig. 4e–g. Based on EDX mapping, Ti, C and O dispersed uniformly in and through the nanocomposites. The bright field TEM image of TiO₂/C, as shown in Fig. 4h, confirms formation of mesopores with a diameter of approximately 10–20 nm. Low magnifications TEM images also confirmed the presence of macropores as shown in Fig. S3. The selected area diffraction pattern (SAED) in the inset of Fig. 4h confirms poly-crystalline structure of TiO₂. The TiO₂/C nanocomposites were further studied via high resolution TEM. The lattice spacing of TiO₂ crystalline was measured to be 0.35 nm, which corresponds to the (101) plane of anatase.

The surface area and pore structure of TiO₂/C composites prepared from different silica dimensions are shown in Table 2. The adsorption-desorption isotherms of nitrogen as well as the size distribution of pores are shown in Fig. 5. The N₂ adsorption-desorption isotherms of other control samples were shown in Fig. S4. All adsorption-desorption isotherms show characteristics of type IV isotherm due to capillary condensation in the mesopores [39]. The existence H₂ hysteresis loop indicates that the TiO₂/C composites prepared in the current work have interconnected pore structure with both micro- and mesopores [40]. Compared with TCS0, all other samples showed increased cumulative pore volume (TCS22 was up to 0.38 cm³/g). According to the pore-size distribution in the inset obtained from nitrogen adsorption by the NLDL model, it can be clearly noticed that the mesopores were formed in the TiO₂/C nanocomposites with sizes 7 nm, 10 nm and 18 nm for TCS7, TCS12 and TCS 22. The total surface area of all TCS samples increased from 263 m²/g to 330 m²/g with increase in silica size from 0 to 22 nm. The surface area and pore volume of mesopores also increased from TCS0 to TCS22. The above results showed that the total surface area and the surface area and volume of mesopores increased with addition of silica during fabrication of TiO₂/C nanocomposites. The pore structure as well as volume/surface area of mesopores is tunable by adjusting the dimension of the silica template during dual-templation synthesis.

In Fig. 6a and b, the photocatalytic reactivity of the TiO₂/C samples was evaluated through the decomposition rate of MB solutions under UV and visible-light exposure. The intensity change of MB from UV-vis spectrometer by TCS22 presented in Fig. S5 was used as an example to illustrate the photocatalytic characterization. Before characterization, an equilibrium state between adsorption and desorption was met for MB and the catalyst. Self-degradation of MB under visible light/UV exposure was evaluated. The corresponding reactivity is negligibly small. Photocatalytic MB decomposition adhered to the pseudo-first-

order reaction [41]. As a comparison, photo-degradation of MB by the control sample P25 was evaluated with the kinetic values listed in Tables S3 and S4.

Based on Fig. 6a and b, the photocatalytic reactivity of TiO₂/C nanocomposites increased from TCS0 to TCS22, indicating samples prepared with silica of large sizes has elevated photocatalytic performances for organic dye degradation. The TCS22 nanocomposites showed the highest photocatalytic reactivity with k values of 0.3344 and 0.0661 min⁻¹ under UV and visible light, which are approximately 4.0 and 10.7 times of the benchmark photocatalyst P25 as well as 16.8 and 10.8 times of anatase. Anatase is commonly known with better photochemical performances compared with rutile, another benchmark photocatalyst, for MB degradation [42]. In contrast, the mechanical mixture of commercial TiO₂ (P25) and carbon with and without annealing did not show increase in photocatalytic activity under either illumination conditions in comparison with their components. The photoelectrochemical response of the TiO₂/C nanocomposites and P25 were investigated and the photocurrent density-potential (J-V) curves ranging from 0 to 1.0 V vs SCE under visible light exposure are presented in Fig. 6c. The current-potential curves in open circuit with and without applying light illumination are shown in the inset. Based on the linear sweep voltammograms, the photocurrent densities of the samples under visible light exposure increased with coarsening of silica in the order of TCS22 > TCS12 > TCS7 > TCS0 > P25, while the corresponding values are 0.9, 2.0, 4.2 and 6.3 mA/cm² with TCS0, TCS7, TCS12 and TCS22, respectively. Furthermore, influences of temperatures and annealing duration on the photochemical activity of TCS22 under both exposure conditions are investigated, as shown in Fig. 6d-f. An increasing annealing temperature leads to increase in the reactivity before 900 °C while further annealing to 1000 °C caused significant reduction in the reaction rate under both irradiation conditions. Based on data shown in Fig. 6f, 5-h is selected as the optimum annealing time for processing the nanocomposites with the highest photocatalytic activity presented. The annealing duration will affect the phase composition, pore structure, surface area and other microstructure related factors, which can induce change in photocatalytic performances. Photo-stability of TiO₂/C nanocomposite is also evaluated with data shown in Fig. 7. The photocatalytic reactivity of TCS22 maintained unchanged even after 5 testing cycles, confirming excellent stability of TiO₂/C nanocomposites prepared in the current work.

In the current work, a novel and feasible method for tuning of the pore structure of metal oxide/carbon nanocomposites prepared from the dual-templation method with high photocatalytic and photoelectrochemical performances is proposed. By using silica as the hard template combined with ice templation, the mesopore size of TiO₂/carbon nanocomposites with hierarchical pore structures at three different length levels has been optimized with influence on the photochemical reactivity revealed. The excellent photochemical performance of the TiO₂/carbon nanocomposites prepared in the current work is attributed to combination of multiple factors including high surface area, appropriate phase composition and annealing condition, pore size distribution as well as robust interface, etc. The weakened reactivity of the annealed mechanical mixture reveals that the interfacial chemical bonding between components is not the sole contribution for enhancement of the photocatalytic reactivity of the materials. The unique microstructure and surface morphology of the prepared TiO₂/C nanocomposites also contributes to increase in reactivity. The tunable mesopore size is beneficial for adjustment of the surface area and optimization of the interface between the liquid phase and the nanocomposites, leading to efficient separation of charge carriers and enhancement in photochemical properties. In addition, its microstructural feature with combination of micro-, meso-, macro- hierarchical pores altogether in the same framework provides more channels for electrons transfer to electrolytes or organic dyes for photochemical reactions within their lifetime. Meanwhile, it facilitates light harvesting within the nanocomposites by providing more

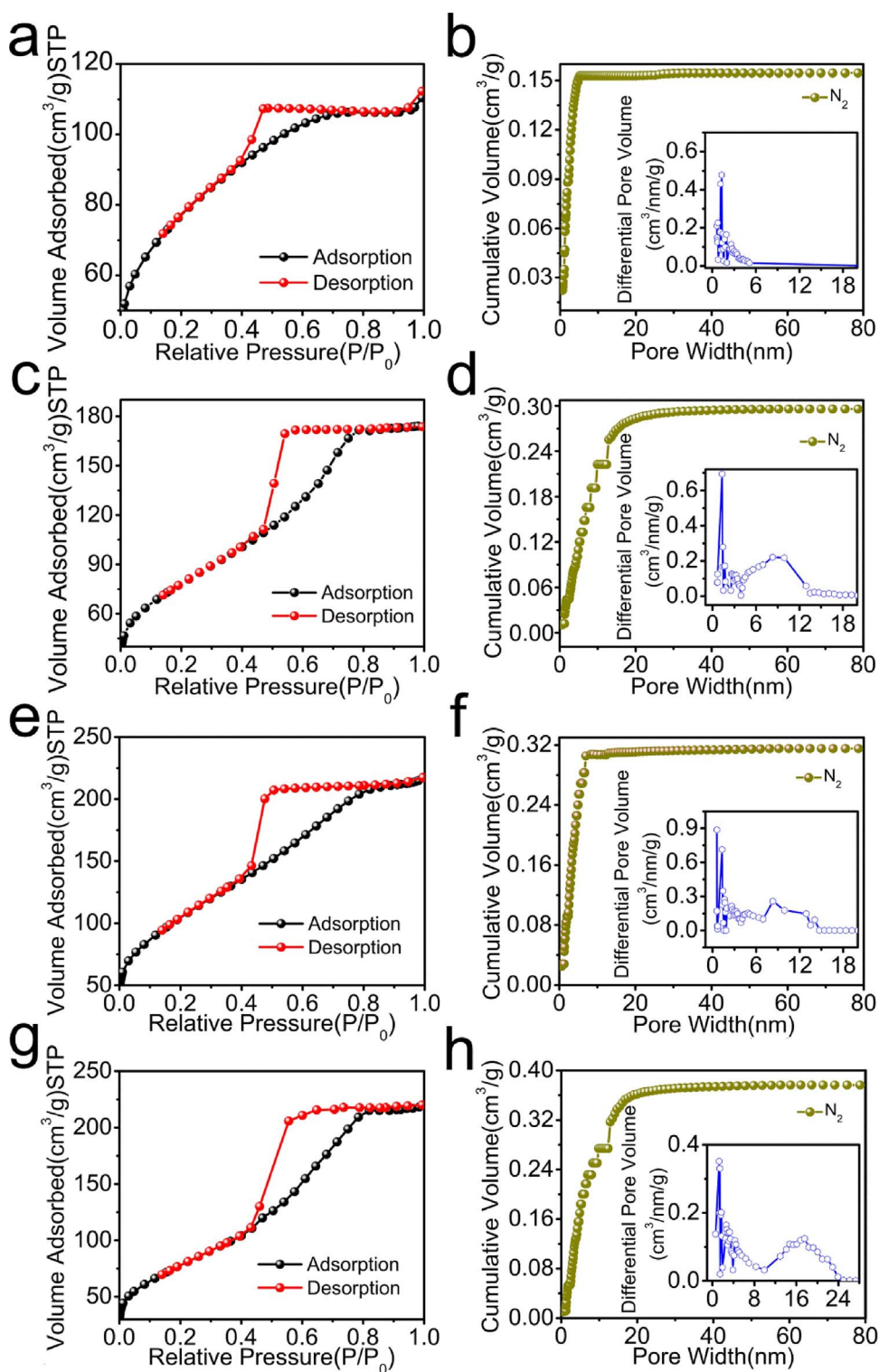


Fig. 5. N₂ adsorption-desorption isotherms as well as the pore volume and pore size distribution (calculated by the NLDFT model) of TiO₂/C with silica templates in the size of (a-b) 0 nm; (c-d) 7 nm; (e-f) 12 nm and (g-h) 22 nm.

absorbed photons. Colloid silica combined with ice templating served as one of the key knobs to adjust formation of mesopores. Furthermore, addition of silica changes the phase composition during synthesis and inhibits phase transformation from anatase to rutile. An appropriate phase composition between anatase and rutile leads to a higher photocatalytic activity for organic dye degradation than single components, such as P25 in which the ratio between anatase and rutile is around 70:30 [42]. The annealing temperature and duration affects the photocatalytic activity significantly through multi-factors, such as phase composition, surface area, interfacial bonding strength between

components, as well as pore size distribution. In general, increase in the annealing temperature coarsens the nanocomposites but also improves the contact between carbon and TiO₂. Influence of the annealing temperature on the photocatalytic reactivity of nanocomposites is a complicated issue requiring optimization of both the annealing temperature and duration. The detailed mechanism is shown in Fig. 8a and b for powdered photocatalysts and photoelectrochemical cells.

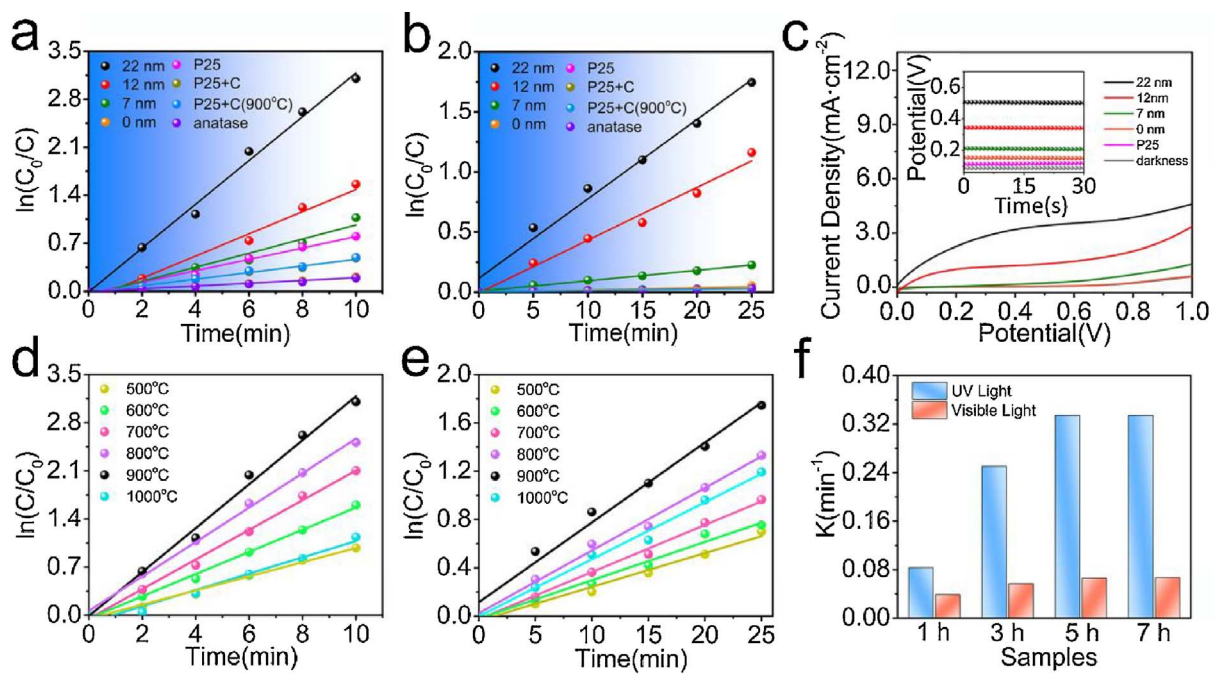


Fig. 6. TiO_2/C nanocomposites annealed at 900 °C with silica templates in different sizes and control samples: (a) (b) photocatalytic degradation of MB under UV and visible light irradiation; (c) photocurrent density-potential (J - V) curves under visible light irradiation. “Dark” corresponds to samples without light exposure; the corresponding open circuit curves are shown in the inset. (d) (e) photocatalytic degradation of MB with TCS22 annealed at temperatures from 500 to 1000 °C under UV and visible light irradiation and (f) the K value for MB photo-degradation of TCS22 under UV and visible light irradiation at different times.

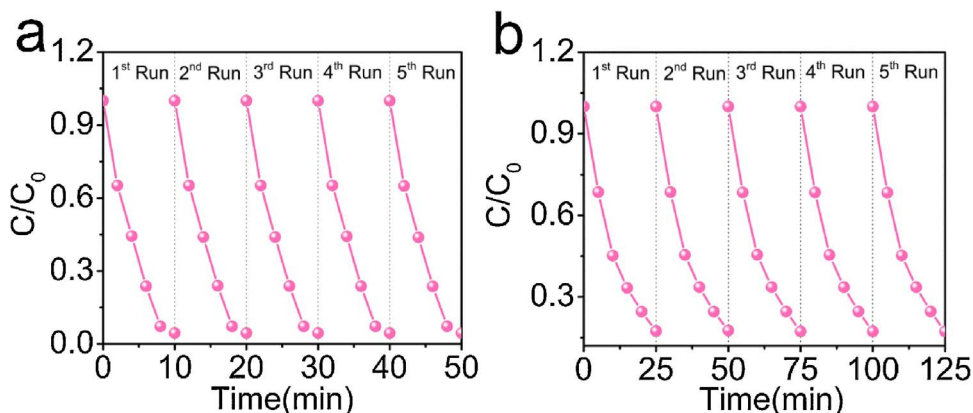


Fig. 7. Recycled photoactivity of TCS22 annealed at 900 °C for MB degradation under (a) UV and (b) visible light irradiation.

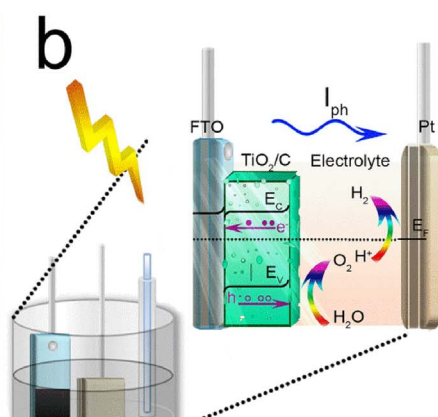
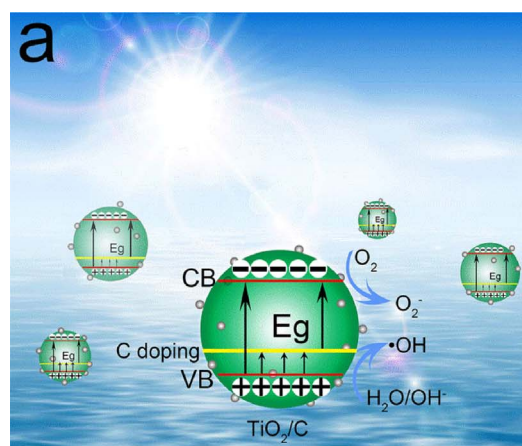


Fig. 8. Schematic illustration of (a) the photocatalytic mechanism of TiO_2/C for MB degradation; (b) transfer path of electrons and holes within the PEC system.

4. Conclusions

In this work, the pore structure of TiO₂/C nanocomposites prepared from dual-templating was tuned by colloid silica with different dimensions. TCS22 showed the ultra-high photocatalytic activity for organic dye degradation, which was approximately 16.8/10.8 times and 4.0/10.7 times of benchmark photocatalysts anatase as well as P25 under UV/visible light exposure. Addition of colloid silica also enhanced phase transformation from rutile to anatase in the nanocomposites. The as-prepared TiO₂/C nanocomposites prepared from the 22 nm silica template showed excellent photoelectrochemical properties with a photocurrent density of 6.3 mA/cm². The influence of annealing temperature and duration on the photochemical properties of the nanocomposites had also been investigated. The photo-reactivity of TiO₂/C nanocomposites was very stable without apparent degradation even after 5 testing cycle. This tactic can be applied to processing of a wide range of metal oxide/carbon materials with different pore structures. Its application can also be extended to energy and electronic related fields for fabrication of high performance functional devices.

Acknowledgement

This work was supported by the National Natural Science Foundation of China (51574062).

Appendix A. Supplementary data

Supplementary data associated with this article can be found, in the online version, at <http://dx.doi.org/10.1016/j.apcatb.2017.10.039>.

References

- [1] L. Li, X. Liu, Y. Zhang, N.T. Nuhfer, K. Barmak, P.A. Salvador, G.S. Rohrer, *ACS Appl. Mater. Interfaces* 5 (2013) 5064–5071.
- [2] G. Li, X. Nie, J. Chen, P.K. Wong, T. An, H. Yamashita, H. Zhao, *Water Res.* 101 (2016) 597–605.
- [3] B.A. Aragaw, C.J. Pan, W.N. Su, H.M. Chen, J. Rick, B.J. Hwang, *Appl. Catal. B: Environ.* 163 (2015) 478–486.
- [4] M. Janus, J. Zatorska, A. Czyżewski, K. Bubacz, E. Kusiak-Nejman, A.W. Morawski, *Appl. Surf. Sci.* 330 (2015) 200–206.
- [5] A. Xiong, G. Ma, K. Maeda, T. Takata, T. Hisatomi, T. Setoyama, J. Kubota, K. Domen, *Catal. Sci. Technol.* 4 (2014) 325–328.
- [6] M. Gao, L. Zhu, W.L. Ong, J. Wang, G.W. Ho, *Catal. Sci. Technol.* 5 (2015) 4703–4726.
- [7] A. Bumajdad, M. Madkour, *Phys. Chem. Chem. Phys.* 16 (2014) 7146–7158.
- [8] H.U. Lee, S.C. Lee, Y.C. Lee, B. Son, S.Y. Park, J.W. Lee, Y.K. Oh, Y. Kim, S. Choi, Y.S. Lee, J. Lee, *Sci. Rep.* 4 (2014) 6740–6748.
- [9] D. Li, J. Jia, T. Zheng, X. Cheng, X. Yu, *Appl. Catal. B: Environ.* 188 (2016) 259–271.
- [10] A. Li, Y. Jin, D. Muggli, D.T. Pierce, H. Aranwela, G.K. Marasinghe, T. Knutson, G. Brockman, J.X. Zhao, *Nanoscale* 5 (2013) 5854–5862.
- [11] P. Zhang, C. Shao, Z. Zhang, M. Zhang, J. Mu, Z. Guo, Y. Liu, *Nanoscale* 3 (2011) 2943–2949.
- [12] X. Shao, W. Lu, R. Zhang, F. Pan, *Sci. Rep.* 3 (2013) 3018–3027.
- [13] Z. Wang, X. Li, H. Xu, Y. Yang, Y. Cui, H. Pan, Z. Wang, B. Chen, G. Qian, *J. Mater. Chem. A* 2 (2014) 12571–12575.
- [14] S. Dutta, A. Bhaumik, C. Kevin, W. Wu, *Energy Environ. Sci.* 7 (2014) 3574–3592.
- [15] L. Rozes, C. Sanchez, *Chem. Soc. Rev.* 40 (2011) 1006–1030.
- [16] C. Sanchez, B. Julián, P. Belleville, M. Popall, *J. Mater. Chem.* 15 (2005) 3559–3592.
- [17] O.J. Hildreth, W. Lin, C.P. Wong, *ACS Nano* 3 (2009) 4033–4042.
- [18] H.Y. Hui, M.A. Filler, *Nano Lett.* 15 (2015) 6939–6945.
- [19] M. Kobayashi, K. Susuki, T. Otani, S. Enomoto, H. Otsuji, Y. Kuroda, H. Wada, A. Shimojima, T. Homma, K. Kuroda, *Nanoscale* 9 (2017) 8321–8329.
- [20] A. Nilchi, S. Janatbar-Darzi, A.R. Mahjoub, S. Rasouli-Garmarodi, *Colloids Surf. A* 361 (2010) 25–30.
- [21] N. Sudhakar, R.K. Singh, S.K. Mishra, S. Kannan, *RSC Adv.* 4 (2014) 49752–49761.
- [22] Y. Li, J. Shen, J. Li, S. Liu, D. Yu, R. Xu, W.F. Fu, X.J. Lv, *J. Mater. Chem. A* 5 (2017) 7055–7063.
- [23] P. Zhang, C. Shao, Z. Zhang, M. Zhang, J. Mu, Z. Guo, Y. Sun, Y. Liu, *J. Mater. Chem. C* 1 (2011) 17746–17753.
- [24] B. Wang, H. Xin, X. Li, J. Cheng, G. Yang, F. Nie, *Sci. Rep.* 4 (2014) 3729–3735.
- [25] M. Zhang, C. Shao, Z. Guo, Z. Zhang, J. Mu, T. Cao, Y. Liu, *ACS Appl. Mater. Interfaces* 3 (2011) 369–377.
- [26] W.W. So, S.J. Moon, *J. Mater. Sci.* 36 (2001) 4229–4305.
- [27] C. Wang, Z. Chen, H. Jin, C. Cao, J. Li, Z. Mi, *J. Mater. Chem. A* 2 (2014) 17820–17827.
- [28] K. Feng, B. Tang, P. Wu, *J. Mater. Chem. A* 3 (2015) 18546–18556.
- [29] G. Wu, X. He, L. Xu, H. Zhang, Y. Yan, *RSC Adv.* 5 (2015) 27097–27106.
- [30] L. Zhang, X. He, X. Xu, C. Liu, Y. Duan, L. Hou, Q. Zhou, C. Ma, X. Yang, R. Liu, F. Yang, L. Cui, C. Xu, Y. Li, *Appl. Catal. B: Environ.* 203 (2017) 1–8.
- [31] Y.P. Tang, D. Wu, S. Chen, F. Zhang, J. Jia, X. Feng, *Energy Environ. Sci.* 6 (2013) 2447–2451.
- [32] D.H. Wang, L. Jia, X.L. Wu, L.Q. Lu, A.W. Xu, *Nanoscale* 4 (2012) 576–584.
- [33] X. Chen, L. Liu, L. Yi, G. Guo, M. Li, J. Xie, Y. Ouyang, X. Wang, *RSC Adv.* 6 (2016) 99695–99703.
- [34] W. Zhou, Y. Liu, Y. Zhang, G. Yang, S. Deng, F. Shen, H. Peng, L. Wang, *New J. Chem.* 38 (2014) 1647–1654.
- [35] L. Hou, H. Hua, H. Cao, S. Zhu, C. Yuan, *RSC Adv.* 5 (2015) 62424–62432.
- [36] F. Cui, L. Xu, T. Cui, T. Yao, J. Yu, X. Zhang, K. Sun, *RSC Adv.* 4 (2014) 33408–33415.
- [37] T. Xu, W. Hou, X. Shen, H. Wu, X. Li, J. Wang, Z. Jiang, *J. Power Sources* 196 (2011) 4934–4942.
- [38] N.P. Huang, R. Michel, J. Voros, M. Textor, R. Hofer, A. Rossi, D.L. Elbert, J.A. Hubbell, N.D. Spencer, *Langmuir* 17 (2001) 489–498.
- [39] Y.W. Zhu, S. Murali, M.D. Stoller, K.J. Ganesh, W.W. Cai, P.J. Ferreira, A. Pirkle, R.M. Wallace, K.A. Cychosz, M. Thommes, D. Su, E.A. Stach, R.S. Ruoff, *Science* 332 (2011) 1537–1541.
- [40] K.S.W. Sing, D.H. Everett, R.A.W. Haul, L. Moscou, R.A. Pierotti, J. Rouquerol, T. Siemieniewska, *Pure Appl. Chem.* 57 (1985) 603–619.
- [41] Y. He, N.B. Sutton, H.H.H. Rijnaarts, A.A.M. Langenhoff, *Appl. Catal. B: Environ.* 182 (2016) 132–141.
- [42] M.S.P. Francisco, V.R. Mastelaro, *Chem. Mater.* 14 (2002) 2514–2518.